PVP-Vol. 489, Problems Involving Thermal-Hydraulics,
Liquid Sloshing, and Extreme Loads on Structures
July 25–29, 2004, San Diego, California USA
PVP2004-3033

NUMERICAL PREDICTION OF HOMOLOGOUS CURVES FOR THE SMART MCP

Min-Hwan Kim, Jong-In Kim, Dong-Ok Kim, Jae-Seon Lee and Jin-Seok Park

Korea Atomic Energy Research Institute
150 Dukjin-dong, Yusong-gu
Taejon, 305-353, Korea
Email: mhkim@kaeri.re.kr Fax: 82-42-868-8990

ABSTRACT

A procedure for generating preliminary homologous curves, which are used as an input for the safety analysis of SMART, was developed. A commercial code for the computational fluid dynamics was adopted as a tool for the procedure. To generate homologous curves, we define the homologous variables and construct a computational matrix. Computations were performed according to the matrix, and the results were compared and analyzed for the representative computational points among the matrix. A modification method to obtain the homologous curves from the results was suggested by using the similarity laws and the complete curves were generated. The curves were compared with available experimental data and the validity of the procedure was investigated.

INTRODUCTION

Development of a pump for SMART (System-integrated Modular Advanced ReacTor), which is called MCP (main coolant pump), has been performed at KAERI (Korea Atomic Energy Research Institute).[1][2][3] Four MCPs, which are axial-flow single-stage canned motor pumps, are installed vertically at the top of the annular cover of the reactor pressure vessel and circulate the reactor coolant from the reactor core to the steam generator cassettes.

The MCP is planned for a prototype manufacture and for its verification test. The objectives of the test are to generate input data for the safety analysis as well as the verification of the MCP performance. Among the data required for the MCP, the homologous curves are representative of the input data which contain not only normal but also abnormal characteristics. These curves are used to analyze the design based events and accidents.

In the SMART, it is impossible to provide the homologous curves from an experiment because the MCP is under development in parallel with the SMART. However, the design branches require the homologous curves of the MCP before the verification test. So we need to develop a procedure for the prediction of the MCP homologous curves.

CFD (Computational Fluid Dynamics) analysis of steady three-dimensional turbulent turbomachinary flows has become more common as the available digital computer speed and memory have increased. So, we adopted the CFD analysis as a substitute for the test. A commercial code for turbo-machinery was used for the analysis.

The purpose of the current study is to develop a numerical procedure for predicting the MCP homologous curves. For this purpose, a computational matrix using homologous variables is constructed and the CFD analysis is performed according to the matrix. A modification method for the CFD results is also suggested. The results are quantitatively analyzed and compared with available experimental data for the validity of the procedure.

NUMERICAL METHOD

FINE/Turbo software[4], which is a commercial code for turbo-machinery, was used for the CFD analysis performed in this study. The code solves Reynolds-averaged Navier-Stokes equations using three-dimensional multi-block structured grids. The discretization in space is based on a second order cell-centered control volume approach using a Jameson et al[5] type of artificial dissipation. The steady-state flow solution is achieved at the convergence of a 4-stage explicit Runge-Kutta time integration scheme. The local time stepping and implicit residual smoothing methods are available to accelerate the residual convergence with a multi-grid strategy. The turbulence modeling may be achieved using various models within the algebraic Baldwin-Lomax model and some linear and non-linear versions of the two-equation k-ε turbulence models. A standard k-ε turbulence model with the wall function[6] was selected for this study.

A. Governing Equations

The Reynolds-averaged Navier-Stokes equations written in a Cartesian frame of the reference, rotating with an angular velocity ω, can be written as

$$\frac{\partial U}{\partial t} + \nabla F_I + \nabla F_V = Q \tag{1}$$

F_I and F_V are respectively the inviscid and viscous flux vectors.

$$U = \begin{bmatrix} \overline{\rho} \\ \overline{\rho \widetilde{w}}_1 \\ \overline{\rho \widetilde{w}}_2 \\ \overline{\rho \widetilde{w}}_3 \\ \overline{\rho \widetilde{E}} \end{bmatrix}, F_{Ii} = \begin{bmatrix} \overline{\rho \widetilde{w}}_i \\ \overline{p^*}\delta_{1i} + \overline{\rho \widetilde{w}}_i \widetilde{w}_1 \\ \overline{p^*}\delta_{2i} + \overline{\rho \widetilde{w}}_i \widetilde{w}_2 \\ \overline{p^*}\delta_{3i} + \overline{\rho \widetilde{w}}_i \widetilde{w}_3 \\ \left(\overline{\rho \widetilde{E}} + \overline{p^*}\right)\widetilde{w}_i \end{bmatrix}, - F_{Vi} = \begin{bmatrix} 0 \\ \tau_{i1} \\ \tau_{i2} \\ \tau_{i3} \\ q_i + \widetilde{w}_j \tau_{ij} \end{bmatrix} \tag{2}$$

where the subscript, i, in the F_{Vi} expression, is used to denote the derivatives with respect to x_i. The energy and velocity components are density weighted averages. The source term vector Q in Equation (1) contains contributions from the Coriolis and centrifugal forces.

$$Q = \begin{bmatrix} 0 \\ -\overline{\rho}\left[2\vec{\omega} \times \vec{\widetilde{w}} + (\vec{\omega} \times (\vec{\omega} \times \vec{r}))\right] \\ \overline{\rho}\vec{\widetilde{w}}\Delta(0.5\omega^2 r^2) \end{bmatrix} \tag{3}$$

In the turbulent case, both the static pressure and the total energy contain contributions from the turbulent kinetic energy k and are defined as

$$\overline{p^*} = \overline{p} + \frac{2}{3}\overline{\rho}k, \quad \widetilde{E} = \widetilde{e} + \frac{1}{2}\widetilde{w}_i \widetilde{w}_i + k \tag{4}$$

The stress and the heat flux components are given by

$$\tau_{ij} = (\mu + \mu_t)\left[\frac{\partial \widetilde{w}_i}{\partial x_j} + \frac{\partial \widetilde{w}_j}{\partial x_i} - \frac{2}{3}\frac{\partial \widetilde{w}_i}{\partial x_i}\delta_{ij}\right] \tag{5}$$

$$q_i = (\kappa + \kappa_t)\frac{\partial \widetilde{T}}{\partial x_i} \tag{6}$$

B. Turbulence Model

The eddy viscosity μ_t in the equation (5) is modeled by a standard k-ε model.

$$\mu_t = \rho C_\mu \frac{k^2}{\varepsilon} \tag{7}$$

$$\frac{\partial(\rho k)}{\partial t} + \nabla \cdot \left[\rho \vec{w} k - \left(\mu + \frac{\mu_t}{\sigma_\varepsilon}\right)\nabla k\right] = H_k \tag{8}$$

$$\frac{\partial(\rho \varepsilon)}{\partial t} + \nabla \cdot \left[\rho \vec{w} \varepsilon - \left(\mu + \frac{\mu_t}{\sigma_\varepsilon}\right)\nabla \varepsilon\right] = H_\varepsilon \tag{9}$$

The source term H_k and H_ε are defined as

$$H_k = P - \rho\varepsilon \tag{10}$$

$$H_\varepsilon = C_{\varepsilon 1} P \frac{\varepsilon}{k} - \rho C_{2\varepsilon}\frac{\varepsilon^2}{k}, \tag{11}$$

where the production terms P are defined as

$$P = \mu_t \frac{\partial u_i}{\partial x_j}\left(\frac{\partial u_i}{\partial x_j} + \frac{\partial u_j}{\partial x_i}\right), \tag{12}$$

and the coefficients are as follows.

C_μ=0.09, σ_k=1.0, σ_ε=1.3, $C_{\varepsilon 1}$=1.44, $C_{\varepsilon 2}$=1.92.

C. Numerical Scheme

The discretization in space is based on a cell centered control volume method and the Equation (1) is discretized as

$$\int_\Omega \frac{\partial U}{\partial t} d\Omega + \sum_{faces} \vec{F}_I \Delta \vec{S} + \sum_{faces} \vec{F}_V \Delta \vec{S} = \int_\Omega Q d\Omega \tag{13}$$

where $\vec{F}_I \Delta \vec{S}$ and $\vec{F}_V \Delta \vec{S}$ are respectively the inviscid and viscous fluxes. The viscous fluxes are determined as purely central. As they contain gradients, gradients must be evaluated on the cell faces. The central scheme with a Jameson-type dissipation is used for the inviscid fluxes.

For the time integration, an explicit multi-stage Runge-Kutta scheme can be written as follows.

$$\begin{aligned} U^{(1)} &= U^{(n)} + \alpha_1 \Delta t F\left(U^{(n)}\right) \\ U^{(2)} &= U^{(n)} + \alpha_2 \Delta t F\left(U^{(1)}\right) \\ &\bullet\bullet\bullet \\ U^{(q)} &= U^{(n)} + \alpha_q \Delta t F\left(U^{(q-1)}\right) \\ U^{(n+1)} &= U^{(q)} \end{aligned} \tag{14}$$

The coefficients α_i determine the stability area and the order of the accuracy of the Runge-Kutta scheme. In this study, the 4 stage scheme is used with the following coefficients.

α_1=0.125, α_2=0.306, α_3=0.587, α_4=1

Local time stepping methods are used to improve the computational efficiency in the calculation of the steady state solutions. Local time stepping means that each computational cell uses a time step which is based on the local numerical stability criterion.

Implicit residual smoothing is also used in combination with the Runge-Kutta scheme to speed up the convergence to a steady state. One-stage in the Runge-Kutta scheme might be written as

$$U^{(m+1)} = U^{(m)} + \alpha_m \Delta t F\left(U^{(m)}\right) = U^{(n)} + \alpha_m R(U^{(m)}) \tag{15}$$

The residual R may be smoothed before applying the update of Equation (15). A smoothed residual $\tilde{R}$ is obtained by applying the following equation.

$$\left(I-\varepsilon_i\Delta_i^2\right)\left(I-\varepsilon_j\Delta_j^2\right)\left(I-\varepsilon_k\Delta_k^2\right)\tilde{R}=R \qquad (16)$$

where

$$\Delta_i^2\tilde{R}=\tilde{R}_{i-1}-2\tilde{R}_i+\tilde{R}_{i+1}.$$

A smoothing parameter ε is calculated from

$$\varepsilon_i=\frac{1}{4}\left[\left[\left(\frac{\sigma^*}{\sigma}\right)\frac{1+\max\left(\sqrt{\left(\lambda_j^*/\lambda_i^*\right)},\sqrt{\left(\lambda_k^*/\lambda_i^*\right)}\right)}{1+\max\left(\lambda_j^*/\lambda_i^*,\lambda_k^*/\lambda_i^*\right)}\right]-1\right] \qquad (17)$$

where σ^* and σ are the CFL numbers of the smoothed and unsmoothed Runge-Kutta scheme respectively and a good practical value is σ^*/σ =2, and the spectral radius is

$$\lambda_i^*=\left[\left(\left|\vec{u}\vec{n}\right|+c\right)\bullet S\right]_i \qquad (18)$$

D. Preconditioning method

In the low subsonic Mach number regime, time-marching algorithms designed for the compressible flows show a pronounced lack of efficiency. When the magnitude of the flow velocity becomes small in comparison to acoustic speeds, the time marching compressible codes converge very slowly.

The problems faced by the compressible codes at a low Mach number are the high disparity between the convective eigenvalues u and the acoustic eigenvalues $u+c$, $u-c$, as well as the round-off errors. The high disparity leads to a very restrictive time step for the convective waves thus causing poor convergence characteristics. The round-off errors are mostly due to the use of an absolute pressure in the momentum equations. Therefore the development of a low speed preconditioner was undertaken in order to provide fast convergence characteristics and accurate solutions as the Mach number approaches zero.

The preconditioned equations considered for a compressible fluid are

$$\frac{1}{\beta^2}\frac{\partial p}{\partial t}+\vec{\nabla}\cdot\left(\rho\vec{w}\right)=0 \qquad (19)$$

$$\frac{\alpha\vec{w}}{\beta^2}\frac{\partial p}{\partial t}+\rho\frac{d\vec{w}}{dt}+\vec{\nabla}p=\vec{\nabla}\cdot\overline{\overline{\tau}} \qquad (20)$$

$$\rho\frac{de}{dt}+p\vec{\nabla}\cdot\vec{w}=\vec{\nabla}\cdot\left(k\vec{\nabla}T\right)+\left(\overline{\overline{\tau}}\cdot\vec{\nabla}\right)\cdot\vec{w} \qquad (21)$$

The above equations can be written in a conservative form as follows and integrated using the numerical method explained previously,

$$\frac{\partial Q_E}{\partial t}+\Gamma_E\vec{\nabla}\cdot\vec{F}=0 \qquad (22)$$

The vector of the dependent variables and the preconditioning matrix are

$$Q_E=\left(p,\ u,\ v,\ w,\ H\right)^T \qquad (23)$$

$$H=C_p\left(T-T_{ref}\right)+\frac{1}{2}\left(u^2+v^2+w^2\right) \qquad (24)$$

$$\Gamma=\begin{bmatrix}\beta^2 & 0 & 0 & 0 & 0\\ -(1+\alpha)u/\rho & 1/\rho & 0 & 0 & 0\\ -(1+\alpha)v/\rho & 0 & 1/\rho & 0 & 0\\ -(1+\alpha)w/\rho & 0 & 0 & 1/\rho & 0\\ \left(\beta^2-\alpha\vec{w}^2-H\right)/\rho & 0 & 0 & 0 & 1/\rho\end{bmatrix} \qquad (25)$$

HOMOLOGOUS CURVES

A common way of plotting the pump performance on a dimensional basis is a family of curves for head (H) or hydraulic torque (T_h) vs volumetric flow rate (Q) at various constant speeds(N), as shown in Figure 1. Expressing each parameter non-dimensionally as a function of the rated value would make the curves applicable to other pumps having similar hydraulic designs but different absolute rated conditions. These parameters normalized by the rated value are called homologous parameters.

$$\nu=\frac{Q}{Q_R},\quad h=\frac{H}{H_R},\quad \alpha_N=\frac{N}{N_R},\quad \beta_h=\frac{T_h}{T_{hR}}\frac{\rho}{\rho_R} \qquad (26)$$

The pump similarity is expressed by the homologous parameters to give

$$\frac{Q/ND^3}{Q_R/N_RD_R^3}=\frac{QN}{Q_RN_R}=\frac{Q/Q_R}{N/N_R}=\frac{\nu}{\alpha_N} \qquad (27)$$

$$\frac{H/N^2D^2}{H_R/N_R^2D_R^2}=\frac{H}{H_R}\left(\frac{N_R}{N}\right)^2=\frac{h}{\alpha_N^2} \qquad (28)$$

$$\frac{T_h/\rho N^2D^5}{T_{hR}/\rho_RN_R^2D_R^5}=\frac{T_h}{T_{hR}}\left(\frac{\rho_R}{\rho}\right)^2\left(\frac{N_R}{N}\right)^5=\frac{\beta_h}{\alpha_N^2} \qquad (29)$$

To the extent that the similarity relationships hold, each family of curves for head or hydraulic torque can be represented by a single homologous curve as shown in Figure 2. Further convenience in plotting data for large values of ν/α_N, especially as α_N approaches zero, is achieved by switching to mathematically equivalent inverse functions when $|\nu/\alpha_N|>1$, i.e., using $\alpha_N\sim\nu$, $h\sim\nu^2$ and $\beta_h\sim\nu^2$. This choice of parameters produces the foldback type of homologous curves shown in Figure 3. For convenient identification of the various branches of the homologous curves, they are labeled HAN, HVN, etc. in accordance with the key shown in Figure 4. As an example, HAN is h/α_N^2 vs ν/α_N for the forward flow and speed.

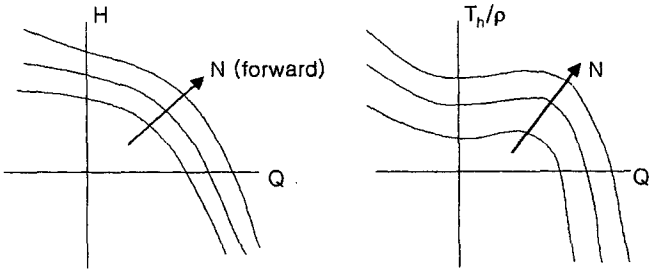

Figure 1. A dimensional pump performance curve

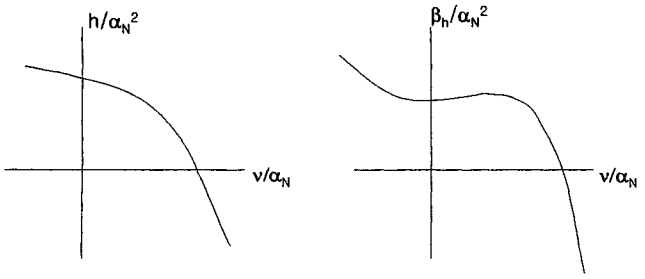

Figure 2. A pump homologous performance curve

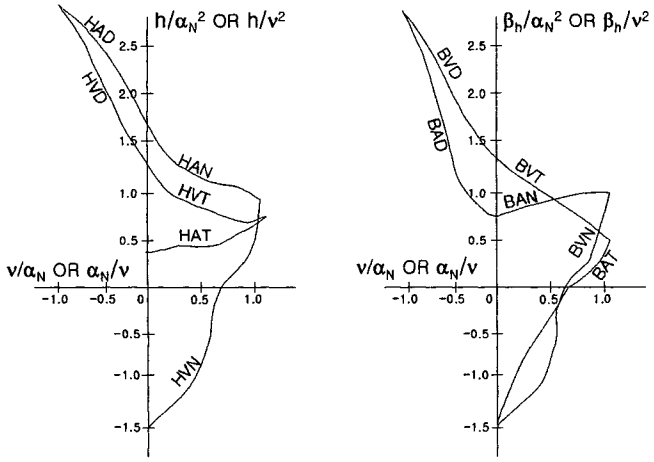

Figure 3. Typical reactor coolant pump homologous curves

H – Head function
B – Hydraulic torque function
A – Function with α_N in denominator
V – Function with ν in denominator, used when $|\nu/\alpha_N| > 1$
N – Normal pumping quadrant with forward flows and speeds
D – Dissipation quadrant with reverse flow and forward speed
T – Normal turbining quadrant with reverse flow and speed
R – Reverse pumping quadrant with forward flow and reverse speed

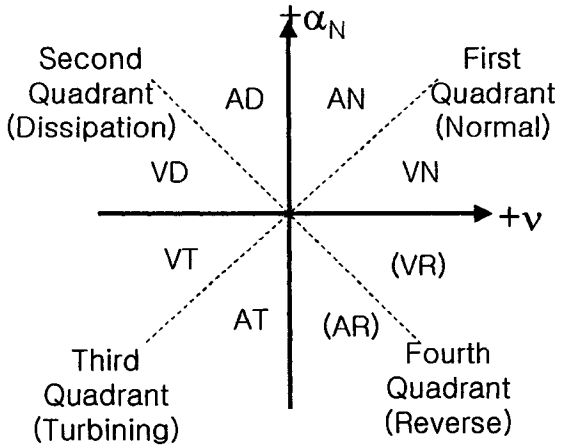

Figure 4. Key to labels on the homologous curves

It is a prerequisite to identify the possible operating region of MCP before generating its homologous curves. The combination of the reverse speed and forward flow (AR and VR regions in Figure 4) is excluded because this region is not significant even in the LOCA analysis.[7] There is no reverse flow because the MCP has a anti-reverse flow device in its discharge. The second and third quadrant in Figure 4, therefore, is not included in the analysis of the SMART MCP homologous curves. As a result, the homologous curves of the MCP being generated in this study are for the first quadrant which includes the head function HAN and HVN, and the hydraulic torque function BAN and BVN.

NUMERICAL COMPUTATION

A. Grid generation

The model pump used in the analysis is an axial type pump designed for a volumetric flow rate of 922m^3/hr and a head of 9m at a speed of 3600 rpm. The designed data for the section profiles of the impeller and diffuser at each radial position are given in Table 1 where R is the radial distance from the axis, l is the chord length , and β_1' and β_2' represent the incidence and discharge angles of the blades.

Table 1. Design values of the impeller and diffuser

<impeller>

R(mm)	38.00	55.11	68.04	78.89	88.41	97.00
l(mm)	57.30	70.08	79.69	86.93	92.72	97.22
thickness/l(%)	12.11	9.88	8.47	7.44	6.65	6.00
β_1'(deg)	58.95	65.51	68.89	70.92	72.16	72.86
β_2'(deg)	15.35	47.09	57.69	63.46	67.41	70.53

<diffuser>

R(mm)	38.00	55.11	68.04	78.89	88.41	98.00
l(mm)	81.78	85.16	86.30	86.88	87.23	87.46
Thickness/l(%)	6.	6.	6.	6.	6.	6.
β_1'(deg)	39.87	29.94	25.00	21.91	19.75	18.12
β_2'(deg)	-6.93	-6.34	-5.98	-5.72	-5.53	-5.37

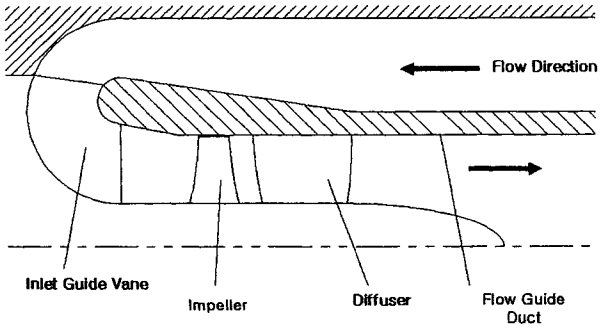

Figure 5. Geometry of the computational domain

Figure 5 shows the geometry of the computational domain where the MCP impeller and diffuser are installed. The numbers of the blades are 5 for the impeller and 9 for the diffuser. The flow comes from the annular space at the outside of the flow guide duct and discharges through the inside of the duct. The MCP has a seven-blade inlet guide vane (IGV) in front of the impeller

To generate the performance curve, we constructed an I-type grid system for the IGV, impeller, and diffuser of the MCP

model. Figure 6 shows a pitch-wise repeated grid system that was generated through the passage including the IGV, impeller, and diffuser blades. The grid system is divided into five blocks, which are the regions for the IGV, impeller, tip-clearance, diffuser, and discharge, respectively. The grids are 29x33x101 (blade-to-blade, spanwise, axial) for the IGV region, 33x41x85 for the impeller region, 9x9x29 for the tip-clearance region, 29x33x73 for the diffuser region, and 28x33x53 for the discharge region. A total of 334,593 grid points were used and the $y+$ values of the first grid points from the wall are about 10~50 for the design flow rate. The surface grids on the periodic boundaries have matching nodes except for the impeller region. In the impeller region, grid skewness is increased due to the highly staggered blades and results in an increase of the numerical analysis error. The use of a non-matching boundary allows for an aligning of the grid lines, as best as possible, with the blade passage flow and reduces the skewness.

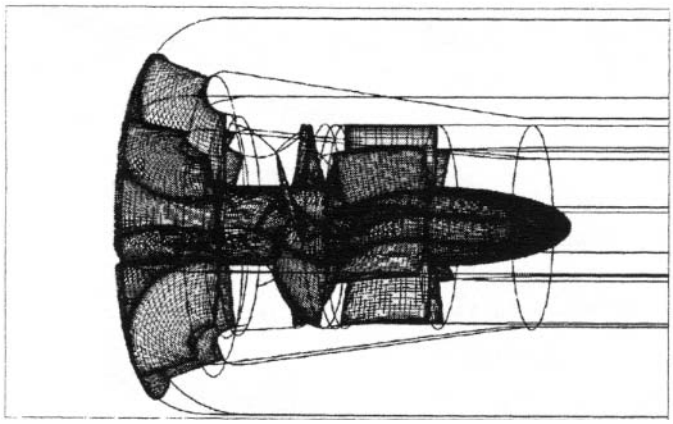

Figure 6. Computational grids

B. Computational matrix

To obtain the capacity-head performance curve of the MCP, we selected the computational points for 5%, 10%, 25%, 40%, 55%, 70%, 85%, 100%, 110% and 120% of the rated capacity (volumetric flow rate). These points include a part of the VN region as well as the AN region. To calculate the rest of the VN region, the computational points were constructed by changing the speed and the capacity. The constructed computational matrix is shown in Table 2.

Table 2. Computational matrix for generating homologous curves

N(rpm)	3600	3600	3600	3600	3600	3600	3600	3600	3600
Q(%)	5	10	25	40	55	70	85	100	110
α_N	1	1	1	1	1	1	1	1	1
ν	0.05	0.1	0.25	0.4	0.55	0.7	0.85	1.0	1.1
α_N / ν									0.909
ν / α_N	0.05	0.1	0.25	0.4	0.55	0.7	0.85	1.0	
N(rpm)	3600	3000	2500	1500	1200	800	600	300	0
Q(%)	120	100	100	70	70	50	50	50	30
α_N	1.0	0.833	0.699	0.416	0.333	0.222	0.167	0.083	0
ν	1.2	1.0	1.0	0.7	0.7	0.5	0.5	0.5	0.3
α_N / ν	0.833	0.833	0.694	0.595	0.476	0.444	0.333	0.167	0
ν / α_N									

C. Initial and boundary conditions

The coolant which is the working fluid of the MCP is assumed as incompressible and the properties at the normal operating conditions are

- Density: 702.9 kg/m^3
- Dynamic viscosity: 1.1977×10^{-7}m^2/s

For the inlet boundary condition, a fixed velocity for each flow rate is used and the turbulent kinetic energy k and dissipation rate ε are calculated from the following.

$$V_{inlet} = \frac{Q}{3600\pi(r^2_{shroud,inlet} - r^2_{hub,inlet})} \quad (30)$$

$$k = 1.5 \times (I_t V_{inlet})^2 \quad (31)$$

$$\varepsilon = C_\mu \frac{\mu}{\mu_t} \frac{\rho_{ref} k^2}{\mu} \quad (32)$$

where the values for the turbulent intensity(I_t) and the viscosity ratio(μ_t / μ) are 0.05 and 50 respectively.

At the outlet boundary, the static pressure is fixed and the others are extrapolated from the interior values. The no-slip condition was specified on the wall. The wall static pressure was calculated by using the normal momentum equation. The impeller region is computed in the rotational reference frame and the other regions in the fixed reference frame. The mixed plane method is used for the interfaces between the blocks. For example, the radial distribution of the static pressure at the exit of the IGV region is obtained from the impeller flow field and all the other flow variables are extrapolated from the IGV interior solution. For the impeller region, radial distributions of all the flow variables at the inlet of the computational domain are obtained from the IGV solution. For further information about the boundary conditions used in this study, consult to reference [4].

RESULTS AND DISCUSSION

A. Comparison of the flow patterns

To investigate the flow characteristics of the MCP homologous curves, the flow patterns at the design point and two representative computational points selected from the AN and VN regions are compared. The value of ν/α_N or α_N/ν is 1 for the design point, 0.55(3600rpm, 55% capacity) for the AN and 0.4762(1200rpm, 70% capacity) for the VN.

The Figures 7, 8 and 9 show the static pressure distributions on the wall. In Figure 7, the pressure at the IGV shroud has lower values due to the more rapid direction change occurring at the shroud than at the hub. On the impeller, it shows similar pressure distributions along the chord line at the radial position except for the tip region. A mild pressure variation through the diffuser implies that it performs its role as a flow guide well without any large energy losses.

Figure 8 is for the AN region where the flow rates are lower than the design point. When reducing the flow rates, the head initially increases due to the increase of flow incidence angle approaching the blade of the impeller which makes the pressure difference between its pressure and suction surface larger. When the flow rate is more reduced and reaches a

critical value, the impeller enters the operation mode with a boundary layer separation along the suction side of the impeller blade. In the much lower flow rate, the separation region grows larger and moves forward. The separation phenomenon makes the lowest pressure region on the middle of the impeller surface in Figure 7 move forward in Figure 8.

According to the similarity law, the volumetric flow rate of 70% at the speed of 1200 rpm in Figure 9 is mapped to 210% at 3600rpm. When the flow rate is increased, the flow incidence angle approaching the impeller is decreased. This results in the decrease of the head generation. At the much higher flow rate, the impeller does not contribute to the generation of a head and only exists as a flow resistance. In Figure 9, the suction surface has a high pressure distribution at the suction surface of the impeller compared to Figure 7 and there is no head increase throughout the impeller.

Flow path-lines through the IGV, impeller and diffuser for the three cases are shown in Figures 10, 11 and 12. The path-lines of the impeller region are for the rotational frame of the reference and the others are for the inertial frame. In Figure 10, the flow throughout the passages is stable but the tip region shows a distinctive feature of the axial turbo-machinery flow. There is a high speed leakage flow, called vortex roll-up, due to the pressure difference between the suction and pressure surfaces of the impeller blades. The flow around the tip region is affected by the vortex roll-up and is lagged behind the other flow. Figure 11 for the AN region shows a more complicated flow pattern than the design point. The large flow separation occurs in front of the impeller and affects the flow entering the diffuser. In Figure 12, the incoming flow to the impeller directly impinges on the suction surface. This makes a high pressure distribution on the suction surface and results in the decrease of the pump head rather than a generation. The flow in the diffuser is also disturbed and contributes to the head loss.

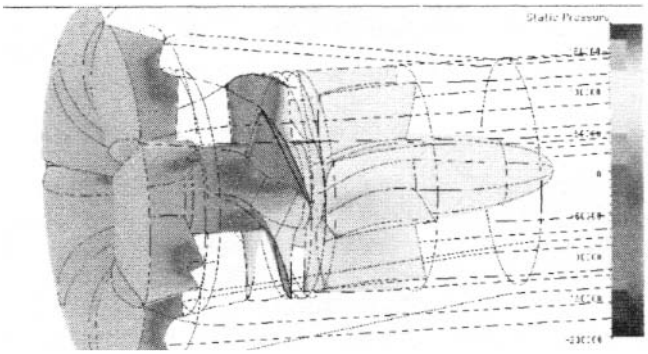

Figure 7. Static pressure distribution at the design point

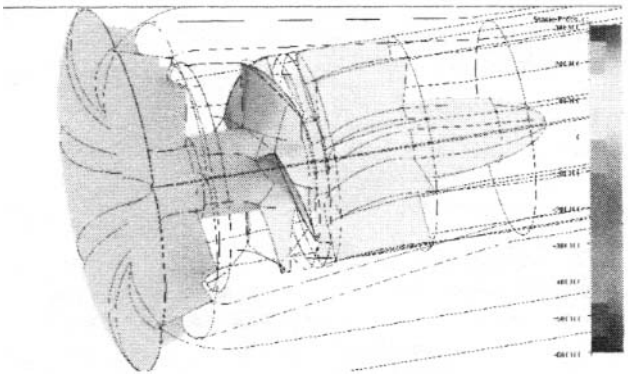

Figure 8. Static pressure distribution at ν/α_N =0.55

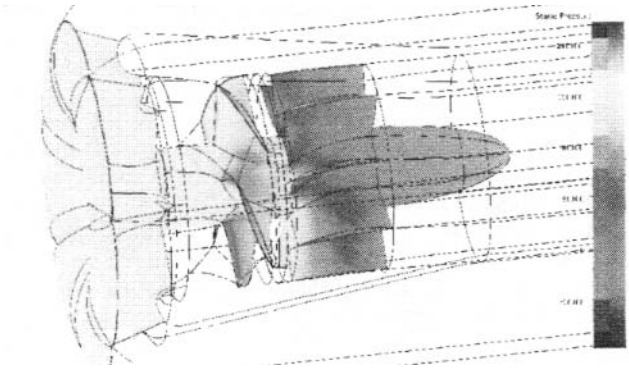

Figure 9. Static pressure distribution at α_N/ν =0.4762

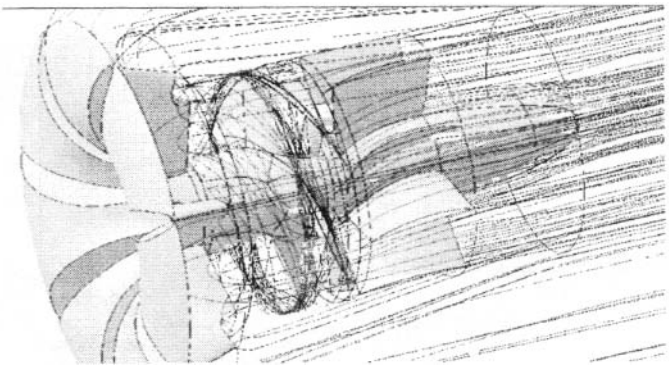

Figure 10. Flow path-lines at the design point

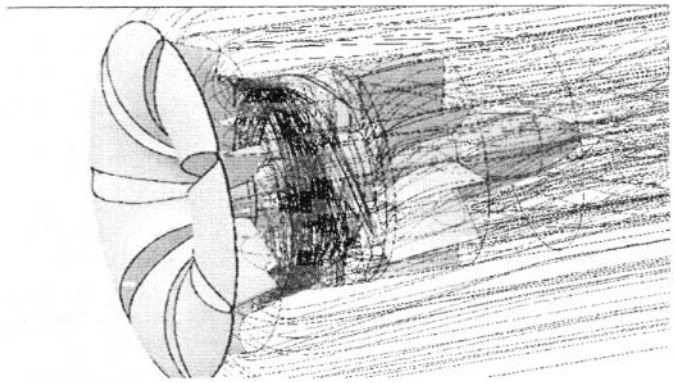

Figure 11. Flow path-lines at ν/α_N =0.55

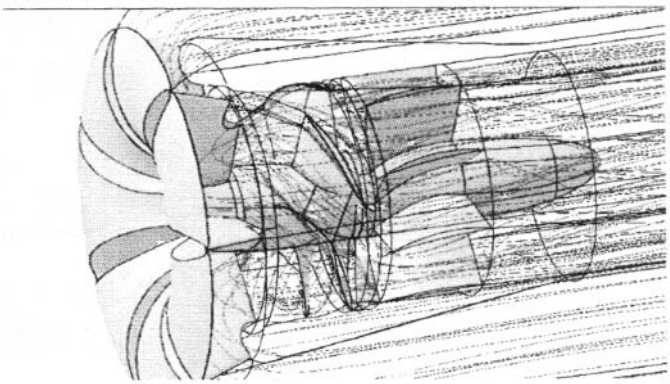

Figure 12. Flow path-lines at α_N / ν =0.4762

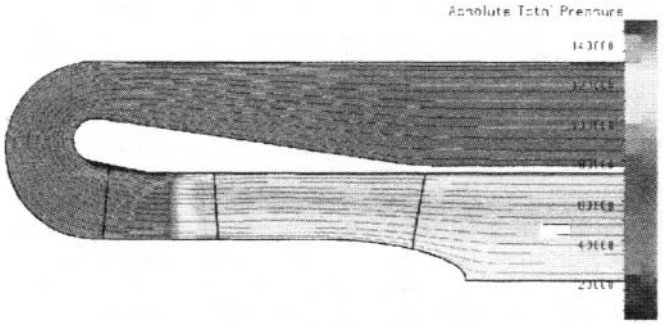

Figure 13. Comparison of the total pressure and flow distributions at design point

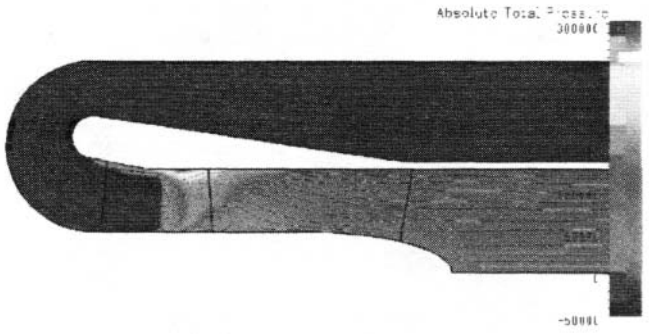

Figure 14. Comparison of the total pressure and flow distributions at ν / α_N =0.55

Pitch-wise averaged total pressure and flow distributions projected on the meridional plane are represented in Figures 13, 14 and 15. Total pressure, which is the sum of the static and total pressures, is directly connected to the pump head. At the design point in Figure 13, the flow pattern and pressure distribution are very stable except for a local decrease of the

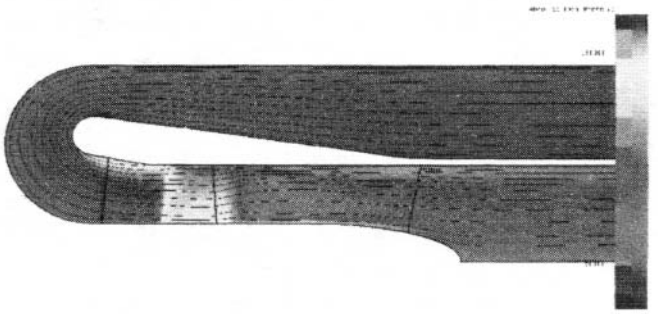

Figure 15. Comparison of the total pressure and flow distributions at α_N / ν =0.4762

pressure on the IGV shroud making the boundary-layer thicker and a vortex roll-up at the tip region. The reverse flow in front of the impeller tip region explained in Figure 8 and 11 is clearly shown in Figure 14. There is another separation at the hub region of the diffuser because the separation at the tip makes the inflow angle for the diffuser disturbed. In the VN region (Figure 15), there is no distinguishable separation although most of head losses are occurring in the impeller.

B. Homologous Curves

The results of the numerical computations according to the matrix in Table 2 are summarized in Table 3. The head is calculated from the total pressure difference between the inlet and outlet.

$$H = \frac{\Delta P_t}{\rho g}$$

Seeing the result at the rated (or design) condition where the capacity is 922m^3/hr and the speed is 3600 rpm, the head is about 10.5m which is larger than the rated one of 9m. If the

Table 3. Computational result for generating homologous curves

N (rpm)	Q (%)	Q (m^3/hr)	ΔP_t (Pa)	H (m)	T (N-m)	Q_1 (m^3/hr)	H_1 (m)	T_1 (N-m)	α_N	ν	h	β_h	ν/α_N or α_N/ν	h/α_N^2 or h/ν^2	β_h/α_N^2 or β_h/ν^2
3600	5	46.1	229878	33.34	168	44.6	32.6	159	1	0.048	3.606	2.855	0.048	3.606	2.855
3600	10	92.2	223490	32.41	163.2	89.2	31.7	154	1	0.097	3.506	2.773	0.097	3.506	2.773
3600	25	230.5	189409	27.47	136.3	223	26.9	129	1	0.242	2.971	2.316	0.242	2.971	2.316
3600	40	368.8	154112	22.35	112.6	357	21.9	107	1	0.387	2.417	1.913	0.387	2.417	1.913
3600	55	507.1	132430	19.21	97	491	18.8	91.8	1	0.532	2.077	1.648	0.532	2.077	1.648
3600	70	645.4	122300	17.74	94	624	17.3	88.9	1	0.677	1.918	1.597	0.677	1.918	1.597
3600	85	783.7	103512	15.01	77.7	758	14.7	73.5	1	0.822	1.624	1.32	0.822	1.624	1.32
3600	100	922	72108	10.46	62.57	892	10.2	59.2	1	0.967	1.131	1.063	0.967	1.131	1.063
						922	9.04	55.7	1	1	1	1	1	1	1
3600	110	1014.2	47339	6.865	51.53	981	6.72	48.8	1	1.064	0.743	0.876	0.94	0.656	0.773
3000	100	922	13767	1.997	22.08	892	1.95	20.9	0.833	0.967	0.216	0.375	0.861	0.231	0.401
2500	100	922	-38779	-5.62	-13.66	892	-5.5	-12.9	0.694	0.967	-0.608	-0.232	0.718	-0.65	-0.248
1500	70	645.4	-35779	-5.19	-17.49	624	-5.08	-16.5	0.417	0.677	-0.561	-0.297	0.615	-1.224	-0.648
1200	70	645.4	-55874	-8.1	-31.03	624	-7.93	-29.4	0.333	0.677	-0.876	-0.527	0.492	-1.911	-1.15
800	50	461	-31794	-4.61	-17.74	446	-4.51	-16.8	0.222	0.484	-0.499	-0.301	0.459	-2.132	-1.289
600	50	461	-43868	-6.36	-25.73	446	-6.22	-24.3	0.167	0.484	-0.688	-0.437	0.345	-2.941	-1.869
300	50	461	-67267	-9.76	-41.25	446	-9.54	-39	0.083	0.484	-1.055	-0.701	0.172	-4.51	-2.996
0	30	276.6	-32456	-4.71	-20.43	268	-4.6	-19.3	0	0.29	-0.509	-0.347	0	-6.045	-4.122

head is normalized by the rated head, the homologous head h/α_N is 1.162 for $\alpha_N = \nu = 1$. Therefore, we need a correction of the results to be h =1 at $\alpha_N = \nu = 1$. A correction method of the pump curve without regard to its characteristic is to apply the similarity laws written as follows.

$$Q \sim ND^3, \quad H \sim (ND)^2, \quad T_h \sim N^2 D^5 \qquad (33)$$

If we reduce the size of the impeller to decrease the head from 10.46m to 9m at the rated condition, the changed variables are

$$Q_1 = Q_0\left(\frac{D_1}{D_0}\right)^3, \quad H_1 = H_0\left(\frac{D_1}{D_0}\right)^2, \quad T_{h1} = T_h\left(\frac{D_1}{D_0}\right)^5 \qquad (34)$$

By changing the diameter ratio, the computation using the above equations is repeated to obtain the head of 9m at the capacity of 100%. The resulting diameter ratio is 0.989 and the head is 9.04m. The capacity, head, hydraulic torque and their homologous variables are calculated from the determined diameter ratio and are listed in Table 3. The resulting homologous head and torque curves are represented in Figure 16. A part of the head curves is compared with experimental data obtained from a cold functional test of the MCP model [8]. Although the data is confined to the AN region, we can conjecture that the homologous curves generated using the procedure developed in this study is reasonable.

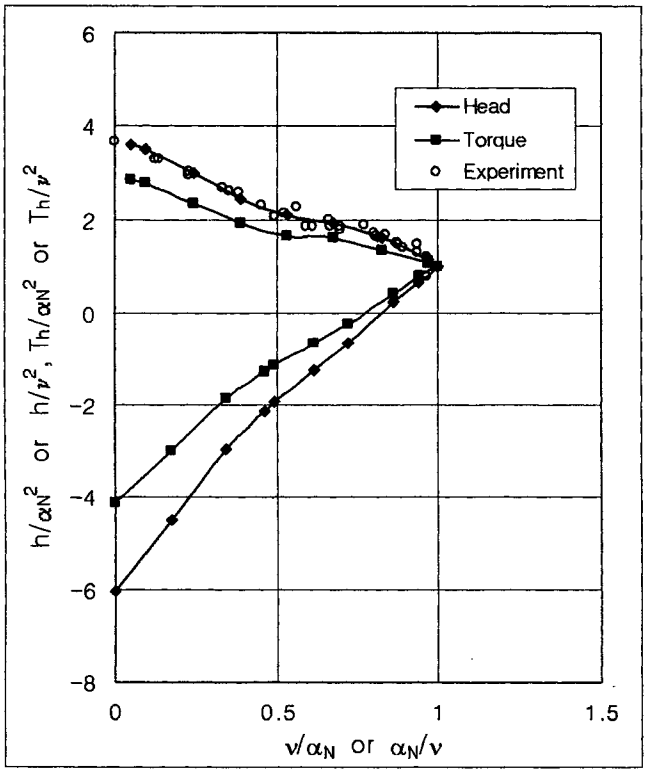

Figure 16. Homologous head and hydraulic torque curves

CONCLUSION

The procedure for generating the MCP homologous curves to be used in a safety analysis was developed and a three-dimensional numerical analysis for a model pump was performed using the FINE/turbo code. For the analysis, a structured grid system was generated including an IGV, impeller and diffuser of the pump, and a computational test matrix was constituted and analyzed.

Among the results, the flow characteristics of the representative flow region on the homologous curves were investigated in detail. At the design point, the flow pattern is very stable except for the tip region which is affected by the vortex roll-up. The AN region having lower flow rates than the design point reveals complex flow characteristics with an increase of the head due to the increase of the incidence flow angle, increase of the size of the flow separation and its forward movement with decreasing flow rates, and another flow separation at the hub region of the diffuser affected by the separation at the impeller. In the VN region, the head is decreased with an increase of the flow rate and the impeller does not contribute to the generation of a head but only flow resistance in the region out of a certain flow rate.

The homologous curves computed from the computational matrix were modified using a dimensional similarity law and a part of the results was compared with the available experimental data. From the results we conclude that the procedure developed in this study for generating homologous curves is reasonable and the curves can be used as a design input for the design branch of a safety analysis.

ACKNOWLEDGMENTS

This work was performed under the auspices of the Korea Ministry of Science and Technology as a long-term nuclear R & D project.

REFERENCES

1. J. S. Park, et al., "Basic Design Report of SMART MCP," KAERI/TR-2135/2002.
2. M. K. Chung, et al., "Development of MCP Impeller Design, Performance Prediction Code and Experimental Verification," KAERI/CM-248/98.
3. H. Huh, J.S. Park and J. I. Kim, "The Design, Fabrication and Characteristics Experiment of Canned Induction Motor of Main Coolant Pump for System-integrated Modular Advance Reactor," IEEE Industry Application Society, OTIM 2002.
4. FINE™ Numeca's Flow Integrated Environment, User Manual, Numeca Inc.,(1999).
5. A. Jameson, W. Schmit, and E. Turkel, "Numerical Solutions of the Euler Equations by Finite Volume Methods Using Runge-Kutta Time-Stepping Schemes," AIAA Paper 81-1259.
6. W. P. Jones and B. E. Launder, "The Prediction of Laminarization with a Two-Equation Model of Turbulence," International Journal of Heat and Mass Transfer, Vol. 15, pp. 301-314, 1972.
7. Pump Two-Phase Performance Program, Volume 2: Steady-state Tests, EPRI Report, NP 1556, 1981.
8. M. H. Kim, et al., "Numerical Analysis of an axial pump performance Including Suction and Discharge for the integral reactor SMART," Proceedings of International congress of Advanced Nuclear Power Plants, Cordoba Spain, 2003.